Supporting Information

Swanson et al. 10.1073/pnas.0908699106

SI Text

Climate Model Evaluation. The 10 climate models examined in this study are: GFDL CM2.0; GFDL CM2.1, HadCM3, ECHAM5/MPI-OM; GISS E-R; Canadian Climate Center; CSIRO; MIROC-MEDRES; MRI; and NCAR CCSM. A brief overview of their various underlying dynamical bases can be found in (1). Preindustrial control simulations were extracted from all 10 models, and the global mean temperature from these simulations was filtered using a third order polynomial with respect to time to eliminate century-scale climate drift in that quantity. A multiple linear regression was then done using the RASST values for the partition elements shown in Fig. 1 and the global mean surface temperature fluctuations in each model's control simulation. This regression is based upon a partition that consists of a series of boxes, each 30° latitude by 60° longitude, spanning 180°W–180°E, 60°S–60°N. Boxes with less than 25% ocean area are excluded, leaving 20 total boxes in the regression. The 5-year running mean in Fig. 1*A* is designed to filter out El Niño/Southern Oscillation variability, which has a dominant period in the 2–5 year range; no time filtering is done in Fig. 2 *A* and *B*. Note that the structure of the weights for the multiple linear regression is not sensitive to the choice of filtering time scale, consistent with a linear approach. This regression yields the weights used in the analysis of Fig. 1*A*. Cross-model validation of the weights was performed; for the eight "active" models described in the primary text, using another model's weights typically explains roughly 50% of the interdecadal temperature variance. An example of such agreement is shown in Fig. S1, which shows the use of the HadCM3 model-derived weights on the ECHAM5 model simulation and vice versa.

For the forced retrospective simulations, an ensemble of identically forced simulations for each model is extracted from the CMIP3 archive. We then calculate the global mean surface temperature for a specific realization relative to each model's ensemble mean, along with the RASST for that realization. Note that the latter is not calculated relative to the ensemble mean, as we seek to test whether forced RASST anomalies confound our approach. The weights derived from the preindustrial controls are then used to predict global mean temperature fluctuations arising solely from SST-associated internal variability. Fig. S2 shows a particular 20th century forced simulation derived from the ECHAM5 model with a spectacular internal event consisting of a 0.4 °C warming over the period 1940–1960, indicated by the deviation of the simulation's global mean temperature from an ensemble mean over many identically forced 20th century simulations. The technique here, using the uniform robust weights of Fig. 1*B*, along with the forced simulation's RASST fields as predictors, identifies that particular 1940–1960 warming event as internal, but significantly, not the greenhouse gas-forced warming post-1960. Hence, our method captures the essence of internal global mean temperature variability, while correctly excluding variability associated with external forcing. Removing that internal variability cleans up the individual forced climate change simulation so that it more closely represents the signal, which in this idealized context is the mean over many different dynamical realizations of the climate model, all with identical forcing.

As indicated in Table S1, this ability extends to the 20th century retrospective simulations (32) considered here. Examination of these 20th century retrospective simulations suggests that our approach is not easily confounded; in 24 of the 32 individual forced simulations from 10 different models examined, the robust weights of Fig. 1*B* act to clean up the individual global mean temperature trajectories, reducing the variance of a given realization's interdecadal global mean temperature from the respective model's ensemble mean on average by 11% (Table S1, column 3). This compares favorably to an optimal statistical model based upon each individual ensemble itself on a model-by-model basis, calculated using the ensemble's RASSTs but now relative to the ensemble mean, along with global mean temperature along with global mean temperature anomalies relative to the ensemble mean to construct a multiple linear regression analogous to that shown Fig. 1. Calculating the weights in this manner captures the maximum amount of variance a linear approach can explain in this context, as there is no forced SST signal to confound the approach. This optimal approach reduces the interdecadal temperature variance from its unfiltered level in 29/32 realizations, with an average variance reduction of 38% (Table S1, column 4). Insofar as the technique here, with the single set of robust weights shown in Fig. 1*B* captures a reasonable fraction of this maximum reduction in variance, these robust weights of Fig. 1, and hence our technique, appear not to be significantly confounded by forced variability.

A final test of the potential for climate change to confound this technique is to apply the robust weights to each model's own climate change pattern. This is done by calculating the linear trend in the RASSTs over the 20th century in each individual simulation. The final column in Table S1 shows the fraction of the global mean temperature anomaly resulting from applying the robust weights to this trend RASST anomaly taken over a century. In most cases, the fractional anomaly is on the order of a few hundredths, that is, by and large climate change RASST anomalies lie nearly in the null space for the robust weights, just as appears to be the case for the observed RASSTs as described in the primary text. Curiously, many of the predicted fractional anomalies are negative, suggesting that internal processes based upon climate change RASST patterns in a sense act to counter the direct global temperature anomaly forced by increasing greenhouse gases.

Linear Discriminant Analysis. Linear discriminant analysis is an approach taken from pattern recognition theory that allows one to identify climate changes that does not hinge on simulations of natural climate variations or estimates of anthropogenic forcing. Observed interdecadal climate variations are decomposed into several discriminants, which are mutually uncorrelated spatio-temporal components with a maximal ratio of interdecadal-to-intradecadal variance. The technique was introduced to the field by Schneider and Held (2) and in the context here provides a purely observational means by which to extract a signal from time-evolving RASST fields. The linear discriminant analysis here is similar to that done by Schneider and Held, with the exception that we define our groups as contiguous 11-year periods, with significant overlap within the groups, spanning the period 1875–2005. The discriminants shown in the Figs. S3 and S4 are not sensitive to this particular definition, however.

Fig. S4*A* shows the RASST pattern associated with the leading discriminant, which should capture the bulk of the anthropogenic climate change signal in that field. This field has the characteristic warming of the southern relative to the northern hemisphere oceans, broadly considered to be the footprint of sulfate aerosols [see (1), chapter 9]. This discriminant has a ratio *R* of interdecadal to intradecadal variance of roughly 6, similar to the ratio for the leading mode for full surface temperature

fields (2). It is vital to note that no time dependence is imposed upon the evolution of this discriminant; despite this, the top panel of Fig. S3 shows that the time evolution of this pattern over the period 1920–2000 is quite linear ($r^2 = 0.92$), specifically much more so than the global temperature itself ($r^2 = 0.67$).

The two higher discriminants that are active in determining internal global temperature anomalies are shown in the bottom panels of Fig. S4, although following Schneider and Held (2) it may not be meaningful to view these discriminants separately as their variance ratios are not widely separated. Mode 2 ($R = 4$), the second leading discriminant, appears to describe a pattern similar to that of the Atlantic Multidecadal Oscillation (AMO), with largest temperature variability found in the North Atlantic/North Pacific. Mode 3 ($R = 3$), the third leading discriminant, appears to resemble the tripole pattern associated with the inter-decadal variability of El Niño, with relatively small RASST anomalies outside the Pacific. Other, higher order discriminants beyond those described here are not associated with significant global mean temperature anomalies. The global mean temperature time series resulting from applying the robust weights of Fig. 1*B* to the time-evolving patterns for modes 2 and 3 are shown in the bottom panels of Fig. S3; Mode 2 has the appearance of a pulse of warming centered on about 1940, while Mode 3 is more oscillatory over the 20th century. The sum of these two time series is what is shown in Fig. 2*B*, and effectively explains the bulk of the 20th century global mean temperature signal arising from internal climate dynamics as shown in the primary manuscript Fig. 1. What is important here is that there is no obvious anthropogenic forcing explanation for these modes, as both discriminants 2 and 3 appear associated with well-known patterns of internal oceanic variability.

1. Intergovernmental Panel on Climate Change (2007) Climate Change 2007: The Physical Science Basis. Solomon S, et al., eds. (Cambridge University Press, Cambridge, United Kingdom).

2. Schneider T, Held IM (2001) Discriminants of twentieth-century changes in Earth surface temperatures. *J Clim* 14:249–254.

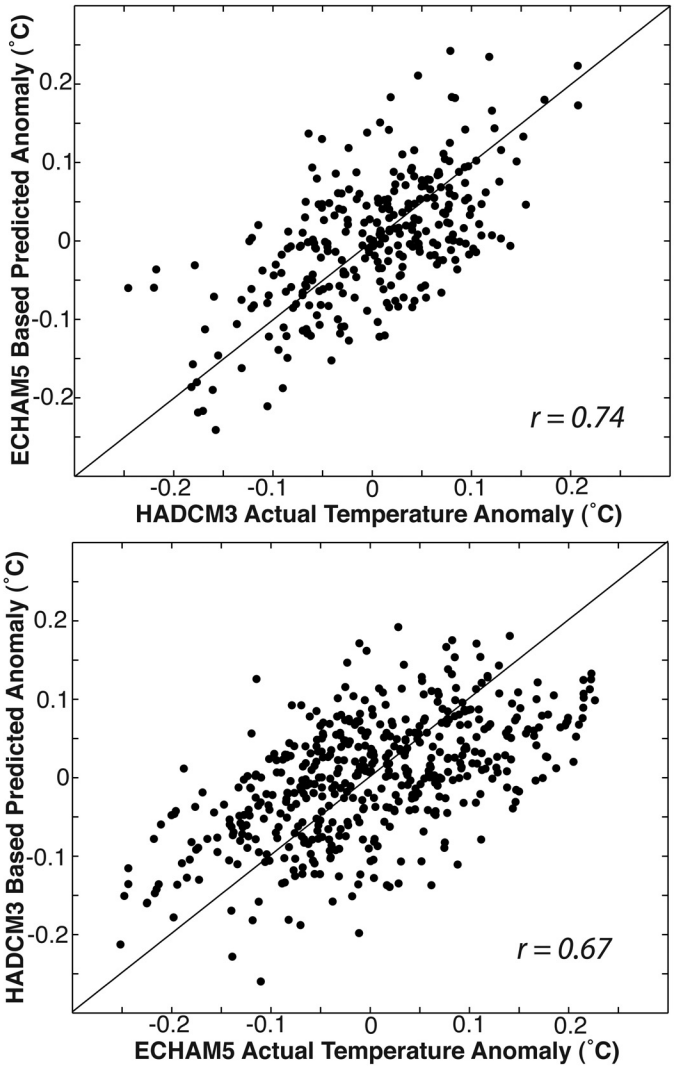

Fig. S1. State-of-the-art climate models have the ability to predict each other's global mean temperature anomalies given only information on internal variability. Here we show cross model predicted (ordinate) and actual (abscissa) global mean temperature anomalies using the multiple linear regression technique acting on residual anomaly SSTs from preindustrial simulations, where internal variability is the only source of anomalies in global mean temperature. In each panel the line indicates perfect predictability. The difference in the number of points corresponds to the difference in preindustrial control simulation length − 500 years for the ECHAM5 model and 340 years for the HADCM3.

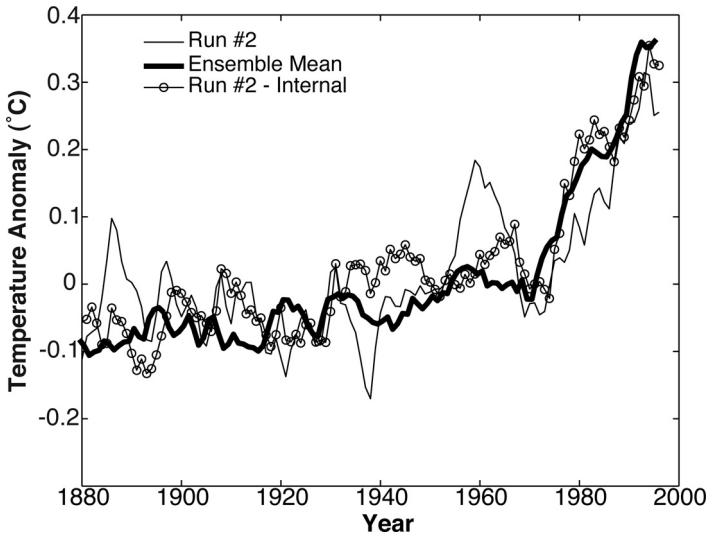

Fig. S2. Internally driven global mean temperature anomalies may also be identified in climate models forced by increasing greenhouse gases and other natural and anthropogenic forcings. Here we show global mean temperatures from simulations using the ECHAM5/MPI-OM model that are intended to mimic the climate of the 20th century. Four simulations using identical forcing are examined; the heavy solid curve is the ensemble mean global mean temperature over all four simulations, and the light solid the global mean temperature for run #2. The line with circles is run #2's global mean temperature cleaned of internal climate variability using the multiple linear regression approach outlined here; it is apparent it more closely resembles the ensemble mean, which is the climate signal in this context.

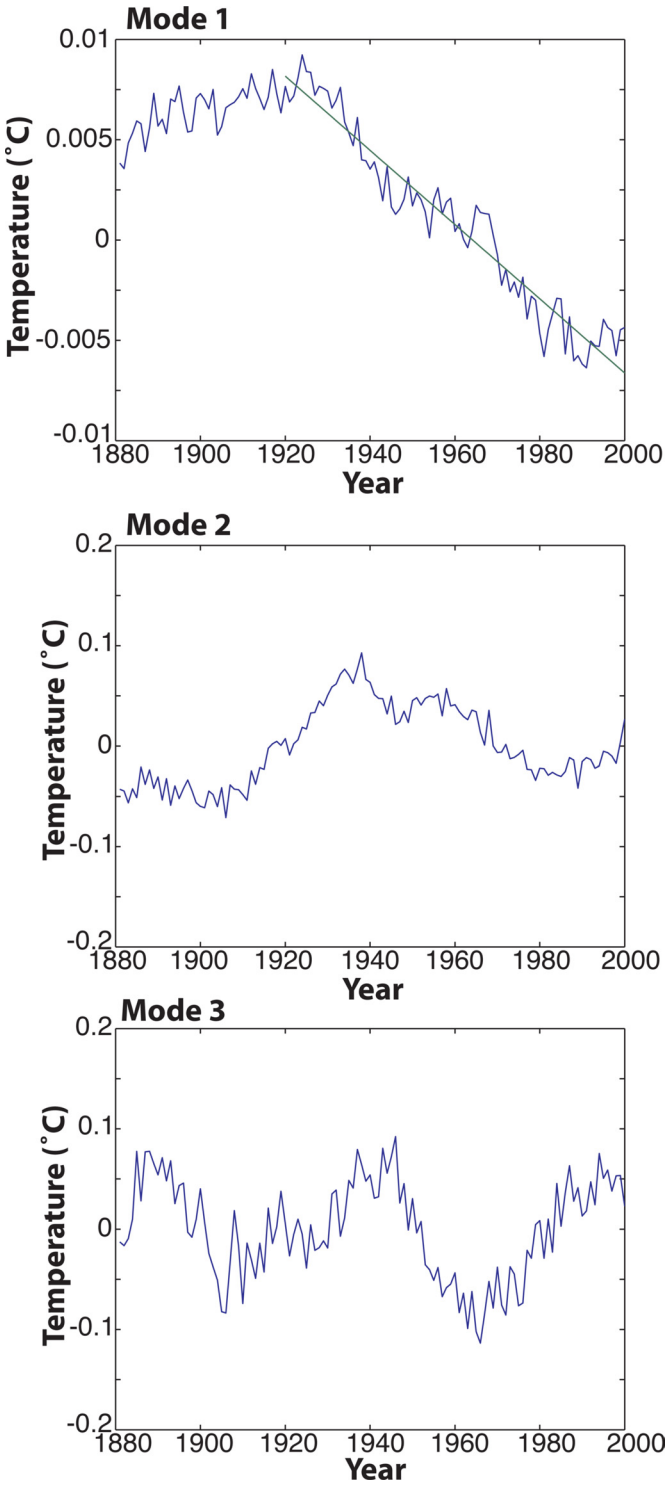

Fig. S3. The global mean temperature signatures associated with the 20th century evolution of the leading linear discriminants shown in the primary manuscript's Fig. 2. The leading discriminant is this techniques estimate of the signature of forced climate change, and is very nearly linear over the period 1920–2000. The other discriminants are oscillatory, and their sum yields the global mean temperature perturbation shown in Fig. 2*B*.

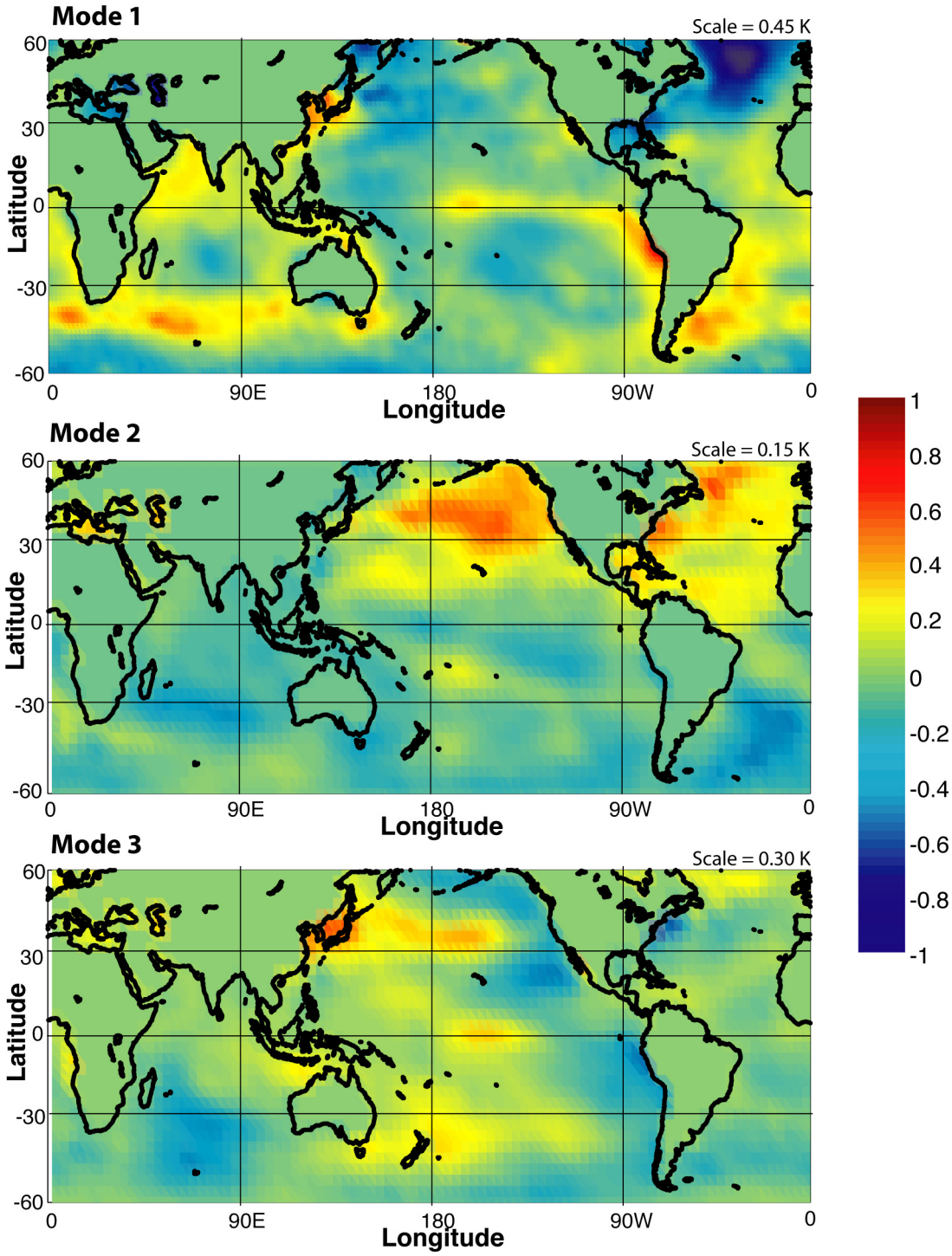

Fig. S4. Global sea surface temperature anomalies associated with the leading three discriminants, with the phase consistent with the year 2000. The leading discriminant (Mode 1) has the characteristic cold Northern Hemisphere/warm Southern Hemisphere pattern consistent with preferential cooling of the North due to sulfate aerosol forcing. The second two discriminants have structures reminiscent of the Atlantic Multidecadal Oscillation (Mode 2) and a Pacific tripole consistent with inter-decadal fluctuations in El Niño (Mode 3). The temperature scale is indicated by the color bar, scaled by the temperature anomaly in the upper right hand of each panel.

Table S1. Standard deviation of decadal-mean global mean surface temperature for thirty-two 20th century retrospective simulations

20c3m Simulations	Decadal STD	Uniform STD	Self STD	Confound
GFDL CM2.1 1	0.050	0.044	0.037	0.014
GFDL CM2.1 2	0.035	*0.037*	0.032	0.012
GFDL CM2.1 3	0.085	0.079	0.062	−0.006
GFDL CM2.1 4	0.091	0.089	0.082	0.046
ECHAM 1	0.043	0.037	0.032	0.001
ECHAM 2	0.052	0.046	0.042	−0.012
ECHAM 3	0.042	0.035	0.031	0.018
ECHAM 4	0.055	0.045	0.042	0.018
GISS 1	0.030	*0.031*	0.021	0.018
GISS 2	0.019	0.018	0.012	0.051
GISS 3	0.029	*0.033*	0.024	0.025
CCC 1	0.030	0.029	0.027	0.025
CCC 2	0.024	*0.025*	0.022	−0.016
CCC 3	0.037	0.034	0.028	−0.001
CCC 4	0.023	0.022	*0.026*	0.011
CSIRO 1	0.041	0.039	0.029	0.064
CSIRO 2	0.035	*0.040*	0.026	0.059
CSIRO 3	0.060	0.051	0.045	0.059
MIROC MEDRES 1	0.039	0.033	0.031	0.031
MIROC MEDRES 2	0.027	0.024	*0.031*	0.031
MIROC MEDRES 3	0.039	0.033	0.028	0.005
MRI 1	0.026	*0.031*	*0.041*	−0.009
MRI 2	0.041	0.035	0.034	−0.028
MRI 3	0.045	0.039	0.028	0.016
NCAR CCSM 1	0.056	0.054	0.036	0.036
NCAR CCSM 2	0.056	0.055	0.034	−0.126
NCAR CCSM 3	0.061	0.047	0.051	−0.01
GFDL CM2.0 1	0.096	*0.099*	0.065	−0.052
GFDL CM2.0 2	0.085	0.072	0.059	−0.045
GFDL CM2.0 3	0.060	*0.063*	0.052	−0.024
HADCM3 1	0.031	0.029	0.027	−0.16
HADCM3 2	0.031	0.024	0.022	−0.12

The column ″Decadal STD″ refers to the global mean temperature standard deviation from the ensemble mean; ″Uniform STD″ refers to the global mean temperature ″cleaned″ of internal variability using the robust weights of Fig. 1*B*; ″Self STD″ refers to the global mean temperature ″cleaned″ of internal variability using each model's individual weights calculated from the ensemble itself; and ″Confound″ measures the fraction of the 20th century global mean temperature change that can be attributed to internal variability, using the robust weights and each realizations RASST patterns.